

JGR Solid Earth

RESEARCH ARTICLE

10.1029/2023JB027043

Key Points:

- Ambient noise interferometry was applied to ocean bottom seismometer data from an active source deployment to invert the shear-wave velocity structure
- A selected time-frequency domain phase-weighted stack was adopted to improve the quality of cross-correlations
- Water content and hydrated layer thickness of the subducting plate were estimated in the southernmost Mariana Trench

Supporting Information:

Supporting Information may be found in the online version of this article.

Correspondence to:

M. Xu,
mxu@scsio.ac.cn

Citation:

Zhang, Y., Xu, M., Xiao, Z., Zhou, Y., Yu, C., Lin, J., et al. (2024). Ambient noise interferometry using ocean bottom seismometer data from active source experiments conducted in the southernmost Mariana Trench. *Journal of Geophysical Research: Solid Earth*, 129, e2023JB027043. <https://doi.org/10.1029/2023JB027043>






Received 6 MAY 2023

Accepted 1 MAR 2024

Author Contributions:

Conceptualization: Yayun Zhang, Min Xu, Zhuo Xiao
Data curation: Yayun Zhang, Yong Zhou, Jian Lin, Xuelin Qiu
Funding acquisition: Min Xu, Hongfeng Yang
Methodology: Yayun Zhang, Chuanhai Yu
Validation: Min Xu
Writing – original draft: Yayun Zhang
Writing – review & editing: Min Xu, Zhuo Xiao, Yong Zhou, Chuanhai Yu, Hongfeng Yang

Ambient Noise Interferometry Using Ocean Bottom Seismometer Data From Active Source Experiments Conducted in the Southernmost Mariana Trench

Yayun Zhang^{1,2} , Min Xu^{1,2} , Zhuo Xiao^{1,2,3}, Yong Zhou^{1,2} , Chuanhai Yu^{1,2}, Jian Lin^{1,2,4,5,6}, Hongfeng Yang⁷ , and Xuelin Qiu^{1,2} 

¹Key Laboratory of Ocean and Marginal Sea Geology, South China Sea Institute of Oceanology, Innovation Academy of South China Sea Ecology and Environmental Engineering, Chinese Academy of Sciences, Guangzhou, China, ²Southern Marine Science and Engineering Guangdong Laboratory (Guangzhou), Guangzhou, China, ³College of Artificial Intelligence, Guangxi Minzu University, Nanning, China, ⁴Department of Ocean Science and Engineering, Southern University of Science and Technology, Shenzhen, China, ⁵Advanced Institute for Ocean Research, Southern University of Science and Technology, Shenzhen, China, ⁶Department of Geology and Geophysics, Woods Hole Oceanographic Institution, Woods Hole, MA, USA, ⁷Earth System Science Programme, Faculty of Science, The Chinese University of Hong Kong, Hong Kong, China

Abstract Ocean bottom seismometers (OBSs) have been used to detect submarine structural and tectonic information for decades. According to signal source controllability, OBS data have generally been classified into active and passive source data categories. The former mainly focuses on the compressional wave (P-wave) velocity inversion and always lacks valid information about the shear wave (S-wave) velocity structure. While the latter provides structural information with limited resolution due to the aperture of the stations. Overcoming the barriers between processing these two data types will allow the reuse of a vast amount of data from active source experiments to explore the submarine S-wave velocity structural properties. Here, we creatively applied ambient noise interferometry to invert the S-wave velocity structure using data from active source OBS deployment conducted in the southernmost Mariana subduction zone, which had already been utilized to detect submarine P-wave velocity structure. Considering the short time duration and relatively low quality of this type of data, a combined method of short-segment cross-correlation and selected time-frequency domain phase-weighted stacking was adopted to obtain stable cross-correlation functions, which were subsequently used to invert S-wave velocity structures. Compared to previous studies using different methods, our result sheds new light on the crust and upper mantle structure of the southernmost Mariana subduction zone. This method could be used to detect more information based on the reutilization of existing active source OBS data.

Plain Language Summary Active source ocean bottom seismometer (OBS) data are usually used to detect P-wave velocity information of submarine areas using signals from air-gun shootings. However, most of the waveform recording ambient noise has yet to be utilized. A large amount of valuable data needs to be fully exploited for the high cost of OBS experiments. In addition, we still lack shear wave velocity information in many critical marine areas due to the rarely picked shear wave phases. However, this information is of great importance for marine tectonic analysis, such as magmatism, dehydration or serpentinization. Using the recorded ambient noise in OBS data from active source experiments can afford the opportunity to obtain shear-wave velocity structures. We adopted different processing methods to calculate high-quality surface wave dispersion data, which were subsequently used to invert shear wave structures in the southernmost Mariana Trench. This method can also provide structural information with a different resolution that is lacking using passive source OBS data.

1. Introduction

Ocean bottom seismometer (OBS) data have long been precious due to the high-cost deployment and unpredictable recovery of equipment and data. The OBS data can be classified into two categories according to different signal sources. The active source OBS (AOBS) seismic experiments with an array of instruments deployed on the seafloor often last a short time duration and are aimed at accessing wide-angle reflection/refraction data from active shots and mainly inverting the compressional wave (P-wave) velocity structures (e.g., He et al., 2023; Takahashi et al., 2008; Wan et al., 2019). While passive source OBS (POBS) experiments with larger apertures

often take months to years, such as in Hawaii (Le et al., 2022; Wolfe et al., 2009), East Pacific Rise (Weeraratne et al., 2007; Yao et al., 2011), central Mariana (Cai et al., 2018; Qiao et al., 2021) and southern Mariana subduction zone (Chen et al., 2022; Zhu et al., 2019, 2021). This data type has been widely used to invert velocity structures using body or surface waves. However, due to the lower recovery rate and higher cost, the quantity of POBS data lies far behind that of the worldwide AOBS profiles.

The AOBS data generally hold high recovery rates due to short deployment times (e.g., 1–3 weeks in general) and have been widely used to detect relatively high-resolution velocity structures of the uppermost part of the oceanic lithosphere using the crustal/upper mantle reflections and refractions. However, active source shooting only takes 1–2 days, and ambient noise recording passive source signals occupy the remainder of the experiment. Numerous AOBS profiles have been conducted worldwide, and this vast data set was typically set aside after the structural inversion using active source signals. Apart from the recording time duration, the essentials of the two kinds of OBS data appear to have no difference as the frequency band mainly depends on the type of seismometer. It would be of great significance to use the passive source signal of the AOBS data to study the submarine structure.

As natural earthquakes may be rare during the deployment of AOBS, ambient noise interferometry (Bensen et al., 2007; Shapiro & Campillo, 2004) could be applied to this kind of data. The method employs continuous waveform (i.e., ambient noise) and suppresses signals from earthquakes and other active sources. For ambient noise tomography, extracting stable and high-quality noise cross-correlation functions (NCFs), that is, empirical Green's functions, is the most fundamental requirement. Usually, at least 1 month of continuous waveform data is required to obtain stationary NCFs (Bensen et al., 2007). Seats et al. (2012) suggested that different time windows, overlaps, and normalizations in cross-correlation could accelerate this process to about half a month of data. For seismic data with high sampling rates from dense arrays, the time needed to obtain stable high-frequency NCFs can be days to hours (Cheng et al., 2021; Mordret et al., 2014). Theoretically, OBS data are better for ambient noise tomography because the data within the objective period band is mainly derived from the interaction between ocean waves and waves or coasts. Therefore, it may be possible to obtain stable NCFs using OBS data with short time durations by adopting advanced methods of cross-correlation and stacking. These NCFs can be used to invert submarine surface wave velocity and further shear-wave (S-wave) velocity structures.

The S-wave structural information and the ratio between P-wave and S-wave velocities are essential for the analysis of many oceanic tectonic activities, such as hydration and magmatism, especially at shallow depths (Huang et al., 2019; Mjelde et al., 2003). Furthermore, the velocity ratio is critical for lithological studies (Mjelde et al., 2003). However, it is still difficult to identify and extract S-wave phases from active source signals, especially for regions with ambiguous layered structures. As a result, the S-wave velocity structure with an equivalent aperture to the P-wave velocity structure is rarely obtained due to the need for converted S-wave phases. The utilization of passive source signals from the AOBS data can fill this gap. Surface wave data extracted from AOBS data are relatively high-frequency due to the short interstation distance. They can be used to invert the S-wave velocity model of shallow depths. The inverted structures are also great complements to results from POBS data, which are typically deployed at greater station spacing and wider apertures and are therefore sensitive to deeper structures.

The AOBS data are usually of poor quality compared to land station data. The timing system, layout direction, and seafloor coupling could not be well-calibrated for each piece of deployed equipment. Furthermore, the diffuse wavefield needed for ambient noise interferometry can be affected by many not well-known local signal sources for short-duration data. Generally, these random signals should be suppressed by stacking over a long time period. Therefore, using the noisy waveform of short-term AOBS data to extract reliable NCFs can be challenging. In this work, we combined different cross-correlation and stacking methods to generate stable NCFs using the AOBS data acquired from the southernmost Mariana Trench, which can be used in the subsequent velocity inversion or waveform modeling. We also utilized the data to extract surface-wave dispersion curves which can then be used to invert 1-D S-wave velocity structures of different regions considering different water depths. Our results demonstrate the feasibility of ambient noise interferometry of the AOBS data and provide new perspectives on the shallow S-wave structure of the southernmost Mariana subduction zone.

2. Tectonic Setting and Data Processing Scheme

Generated by the convergence of the Pacific Plate and the Philippine Sea Plate, the distinct southernmost Mariana subduction zone holds the oldest oceanic crust and the earth's deepest “Challenger Deep” (Figure 1). Unlike

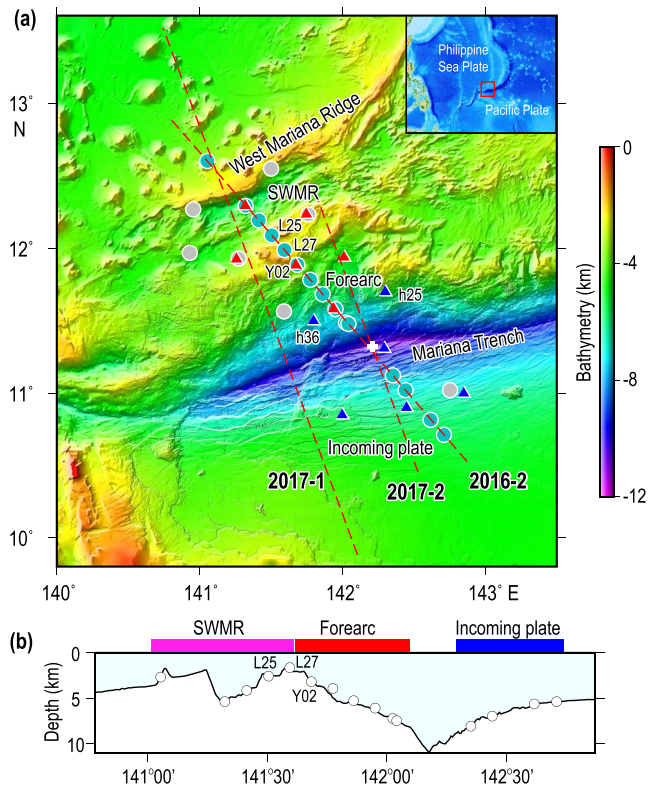


Figure 1. (a) Location of the OBS stations deployed in the southernmost Mariana Trench, of which the data recording was used in this study. The red dashed lines are the wide-angle seismic shooting lines. The cyan circles denote the AOBS station of the profile 2016-2. Off-profile AOBS stations are marked with gray circles. The colored triangles represent the POBS stations, and the stations marked by red triangles were deployed from December 2016 to June 2017, while the blue stations were from March 2017 to June 2017. The deepest point “Challenger Deep” is marked by a white cross. Locations of stations Y02, L27, and L25 are indicated and used to display the data quality improvement shown in Figures 2 and 5. POBS stations h25 and h26 are used in Figure S1 in Supporting Information S1. The study area is outlined by a red box in the inset. (b) Topography of the profile 2016-2 with the locations of the OBSs indicated. The three colored blocks denote the three subregions in which the average S-wave velocity structures are inverted in this study. SWMR: Southwest Mariana Rift.

typical subduction zones, this region lacks a mature arc and suffers diffuse deformation, resulting in spatially distributed forearc segments (Martinez et al., 2018; Sleeper et al., 2021). The Southwest Mariana Rift (SWMR) in the backarc region hasn't undergone much opening and is in a stage of tectonic rifting (Martinez et al., 2018). The active-source seismic profiles 2016-2 and 2017-2 have already been used to invert P-wave velocity slices (He et al., 2023; Wan et al., 2019), which exhibit different features, especially in the uppermost mantle. POBS data (Figure 1) were used to depict the morphology of the subduction slab (Zhu et al., 2019) and to image the forearc and incoming plate using surface wave tomography (Zhu et al., 2021). The inverted S-wave velocity model was utilized to estimate the water content, which differs from the results of earthquake relocation (Emry et al., 2014) and geodynamic modeling (Zhou & Lin, 2018). Furthermore, more precise velocity models are needed to study the subduction tectonics of the southernmost Mariana Trench.

We utilized the data acquired from the southernmost Mariana subduction zone to test the validity of ambient noise interferometry using the AOBS data. Among the several active source wide-angle seismic profiles conducted in the area from 2016 to 2017, we mainly focused on the profile 2016-2 (Figure 1). The obtained P-wave velocity model (Wan et al., 2019) could provide preliminary information for our structural inversion. 22 four-component broadband AOBSs (with an adequate spectrum of $\sim 0.01\text{--}50$ s, indicated by circles in Figure 1 with 15 OBSs along-profile and 7 OBSs off-profile) with 1–2 weeks' deployment duration have been recovered. Along the profile, the interstation distance was initially designed as ~ 15 km except for stations near the trench, and unfortunately, 4 OBSs were not successfully recovered. More detailed information about this along-profile active source experiment can be found in Wan et al. (2019). There are also 12 POBS stations deployed in this region (indicated by triangles in Figure 1). We applied the same procedure to calculate the NCFs and surface wave dispersion data from both AOBS and POBS for comparison.

2.1. Cross-Correlation

The AOBS data mainly features short durations and relatively noisy waveforms due to the design purpose and unknown settlement conditions. Therefore, more improvement of the data quality are needed when processing this kind of data. Before cross-correlation, position and time corrections are necessary (Tian et al., 2021; Wan et al., 2019). The shooting signals from air

guns may affect the frequency band of the continuous waveform, which can be weakened by normalization and whitening. Aimed at relatively high-frequency P-wave phases, the instruments used in the experiments may not comprise the period band used in ambient noise tomography. It is necessary to confirm that the spectrum of the data comprises the objective period band. Fortunately, the broadband instruments we used are appropriate for this work and have been widely used in AOBS experiments (Liu et al., 2022). Figure 2 shows the seismic data's power spectral density and frequency spectrum recorded with one AOBS station. The energy peaks at 2–5 s originated from the secondary microseisms (Ardhuin et al., 2015).

We chose the broad period band of 0.5–20 s to conduct multiple period band cross-correlation considering the interstation distances and the bandwidth of the instruments (Zhang et al., 2018). The pre-processing and normalization followed the traditional ambient noise method (Bensen et al., 2007; Yao et al., 2006). However, the time length of cross-correlation must be shortened from one day to hours to increase the total number of correlated traces before selected stacking. Daily cross-correlation has no scientific justification except for the ease of data access (Abbas et al., 2022; Prieto et al., 2009; Seats et al., 2012). We also tested Welch's method (Welch, 1967) by overlapping the calculated waveform using the optimal parameters from Seats et al. (2012) (Figure 3). To evaluate the quality improvement of NCFs along with the number of stacked data, we used a normalized signal-to-noise

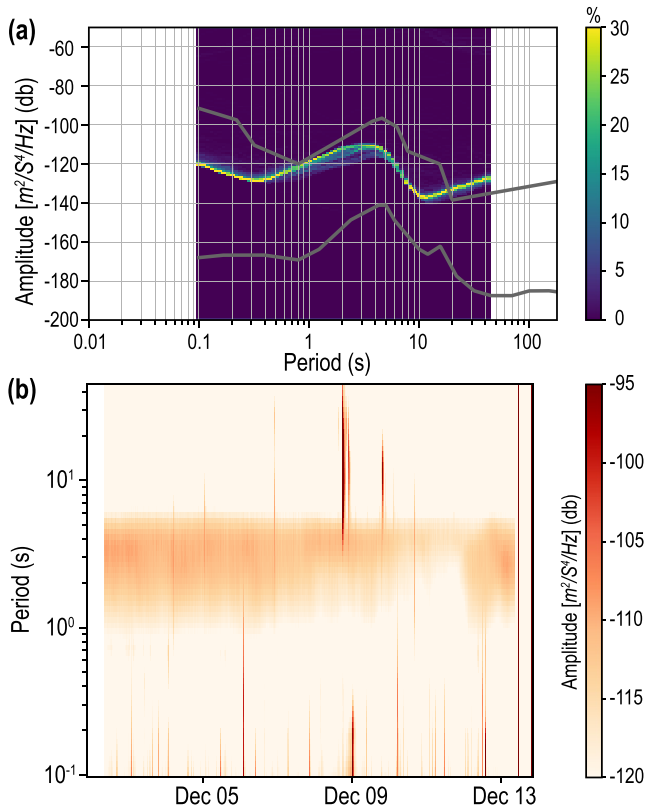


Figure 2. Power spectral density (a) and frequency spectrum (b) of the AOBS station Y02 of which the location is indicated in Figure 1.

ratio (SNR) instead of correlation coefficients between correlated waveform and year-long NCF (Seats et al., 2012) as we only hold 1–2 weeks' data. We defined SNR as the ratio between the mean amplitude of the signal window (1–3 km/s) and the noise window (5–10 km/s) (Zhang et al., 2022). The normalized SNR is defined as:

$$S_i^j = \sum_{k=1}^i \frac{S_k}{S_{\text{final}}^j} \bar{S} \quad (1)$$

S_i^j is the SNR of the data stacked from the first to the i th segment for the j th station-pair, and S_{final}^j is the overall SNR of the j th station-pair. S_k is the SNR of segment k , while \bar{S} is the average SNR of all the station pairs. The changes in window length and percentage of overlap do not significantly affect the quality of the NCFs (Figure 3a). This implication can also be demonstrated by the similar retention rate (about half) of the three data sets that can be used to extract dispersion curves further. This phenomenon mainly results from pre-processing and normalization. In the following process, we chose 3-hr-long segments of the vertical component to do cross-correlation, generating ~100 traces for each station pair, which is sufficient for our subsequent calculations (Figure 3b).

2.2. Stacking

Stacking is an essential procedure in this study. Several methods have been developed to improve the quality of stacking results (Afonin et al., 2019; Cheng et al., 2015; Liu et al., 2021; Moreau et al., 2017; Schimmel et al., 2011; Xie et al., 2020), among which quality selection or weighting is always the critical point. We adopted a combined method by assembling correlation coefficient-based selected stacking and nonlinear time-frequency domain phase-weighted stacking (tf-PWS).

The SNR of linear stacked NCFs does not increase monotonically with the number of stacked segments (Figure 3a), indicating that not all segments of the continuous waveform constructively contribute to the quality of the final NCFs. The main reason might be that the dominant sources of these segments are not located in the stationary-phase zone of the station-pair, as modeled by Xie et al. (2020). The effect of the randomness of sources should be reduced by long-term stacking, which should be more prominent in short-term data studies. Therefore, selection in stacking is more necessary with such data. Xie et al. (2020) used an rms-ratio selected stacking

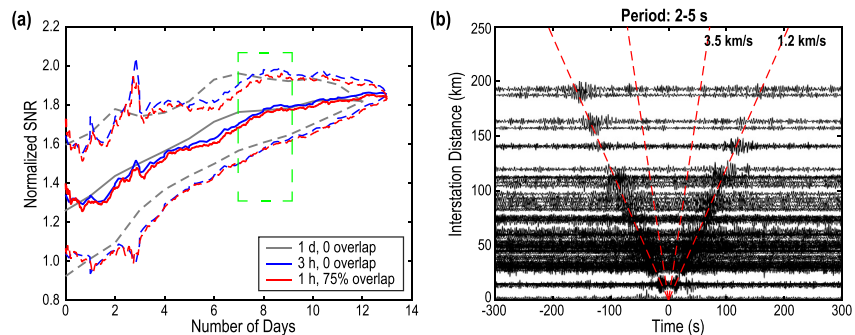


Figure 3. (a) Normalized SNR versus the number of consecutive days stacked for all station pairs with a time length of 13 days. Different color represents different chosen time window length and overlap for the calculation. The gray line denotes daily cross-correlation with no overlap, blue and red represent 3-hr correlation with no overlap, and 1-hr correlation with 75% overlap, respectively. The maximum and minimum values of the normalized SNR are plotted using dashed lines for each. The green dashed box indicates active source shooting during this period. (b) noise cross-correlation functions from 3-hr cross-correlations without overlap and linear stack in the period band of 2–5 s.

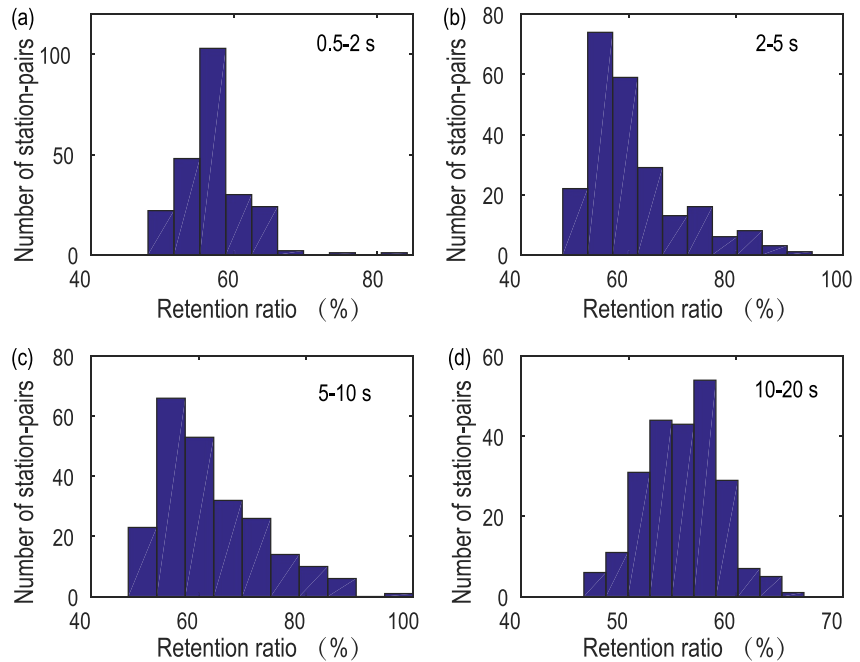


Figure 4. Histograms of the number of station-pairs versus the percentage of retained data after the selection for each noise cross-correlation function according to the normalized correlation coefficient between each trace and the final stacked result. Different period bands are shown in the upper right. The sum of all the numbers represented by each bar is a fixed value $22 \times 21/2 = 231$ (22 stations) for each period band.

method to choose the segment that promotes the SNR of the final NCFs. Our calculation method of SNR may affect the final results as it will generate a manufactured signal in the preset noise window. We used the zero-time lag correlation of the signal window between each correlation and the final stacked results to evaluate the selection step. The normalized correlation coefficient was defined as:

$$C'(f) = \frac{\sum_{i=1}^N x_i(f)y_i(f)}{\sqrt{\sum_{i=1}^N x_i(f)^2} \sqrt{\sum_{i=1}^N y_i(f)^2}} \frac{1}{\overline{C}(f)^\nu} \quad (2)$$

while $x_i(f)$ and $y_i(f)$ are the individual values from two waveforms with the bandpass period band f . $\overline{C}(f)$ denotes the average correlation coefficient for each period band weighted by the parameter ν (set as 1 here). The normalized correlation coefficient could ensure sufficient traces to be stacked regardless of the overall quality of the correlated data. A threshold (set as 0.8 here) was used to select high-quality traces and calculate the percentage of traces retained for each inter-station correlation. The selection procedure was conducted separately in four-period bands as the local sources affecting the quality of NCFs may be frequency and time dependent (Figure 4). Almost all inter-station NCFs retain more than half of the traces in each period band.

This selection step can be iterative to obtain a better stacking waveform. Figure 5 shows the results of a station pair before and after selection using linear stacking (LS). It is obvious that many noisy traces were removed, and a more robust NCF was obtained.

The selected traces were applied to tf-PWS (Schimmel et al., 2011), of which the essence is to put a windowed Fourier transform (S-transform) (Stockwell et al., 1996) into the commonly used phase-weighted stack. This method could further attenuate incoherent noise and enhance the surface wave signal. Thus, cleaned NCFs could be obtained, although more computation time was required. The output waveform in the signal window was more prominent after this stage (Figure 6). We also compared the improvement of the SNR of the NCFs using three different stacking strategies (Figure 7). When we extract dispersion curves from NCFs, the value of SNR should

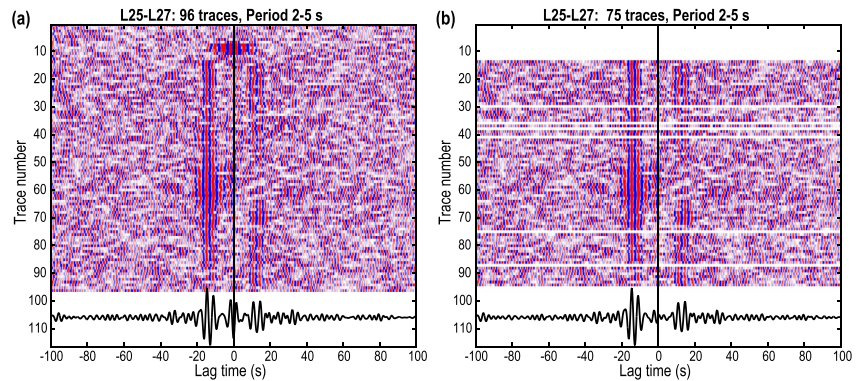


Figure 5. The selection stacking results for the station-pair L25–L27 in the period band of 2–5 s. (a) Linear stack of all traces. (b) Linear stack after discarding traces of low correlation. The locations of stations L25 and L27 are shown in Figure 1.

be at least three empirically. For our AOBS NCFs, the percentages of data that can be used further are ~50%, ~70%, and ~97% for LS, selected LS, and selected tf-PWS, respectively (Figure 7). The combined selected tf-PWS method can significantly enhance the quality of the cross-correlations of the AOBS data. The quality of NCFs could be higher for POBS data using this method (Figure 6c, Figures S1a and S1b in Supporting Information S1). The workflow can also be employed for other low-quality data to obtain robust results that can be used for further modeling or inversion.

3. Inversion and Result

We used the NCFs generated from the AOBS data to extract dispersion curves (Yao et al., 2006; Zhang et al., 2018) and compared them with those obtained from the POBS data. A forward phase velocity dispersion curve based on the averaged 1-D model from Zhu et al. (2021) was employed as a reference. The dispersion curves extracted from the AOBS data appear similar to those from the long-term POBS data (Figure 8),

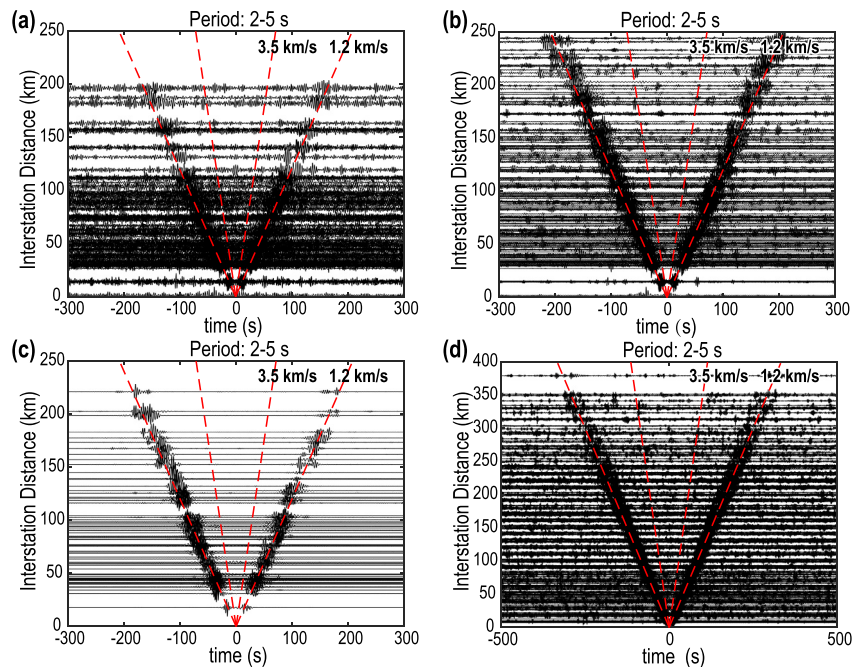


Figure 6. Noise cross-correlation functions (NCFs) from different data sets with SNR greater than 4. (a) NCFs from 3-hr cross-correlation with the selected and linear stack applied to AOBS data from profile 2016-2. (b) NCFs from 3-hr cross-correlation with selected and tf-PWS applied to the same profile 2016-2. 3-hour cross-correlation and selected tf-PWS adopted to (c) the POBS data, and (d) AOBS data from profile 2017-1.

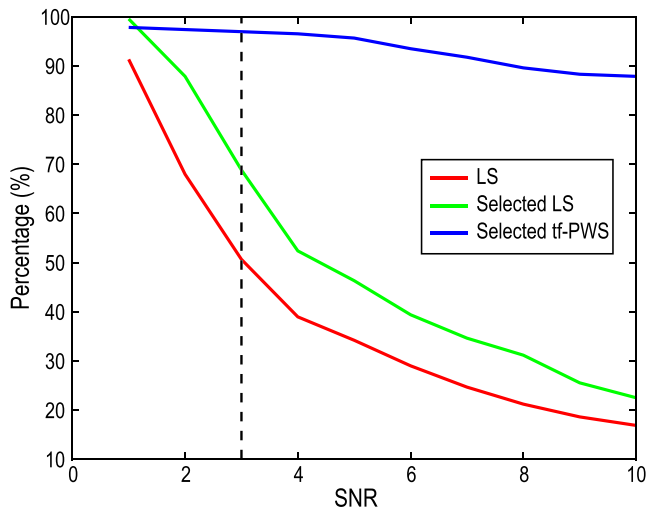


Figure 7. Number of noise cross-correlation functions (NCFs) versus SNR. Different colors denote different stacking methods. The vertical dashed line marks the minimum threshold of SNR = 3 for NCFs, which can be used to extract dispersion data empirically. LS: linear stack, Selected tf-PWS: selected and time-frequency domain phase-weighted stack.

demonstrating the feasibility of using the AOBs data to invert subsurface structures. The difference between the two average dispersion data originates from different geometry configurations of stations. We also compared the dispersion curves of the same station pairs created from the three types of stacking data (LS, selected LS, and selected tf-PWS). The data that can be extracted for each station-pair almost coincide with each other, indicating that no manufactured or spurious signals have been introduced during the process. To verify the validity and effectiveness of the method, we also conducted a test by randomly selecting three segments with a length of 15 days out of the whole waveform for a POBS station-pair (Figure S1 in Supporting Information S1). The dispersion curves extracted from the three segments appear to be of relatively lower quality but similar to the one using all waveforms (Figures S1c and S1d in Supporting Information S1). This proves that the methodology is helpful using the ambient noise of short-term OBS data. The method can significantly increase the path coverage of surface wave measurements as the POBS data is hard and expensive to obtain.

The dispersion data can be used to invert the submarine S-wave velocity structures using Computer Programs in Seismology (Herrmann, 2013). Given the period band of the dispersion data, the topographic relief cannot be neglected here. The water depth of the profile 2016-2 varies from ~2 km to ~11 km in the Challenger Deep (Figure 1). Therefore, the elevation difference can be compared to or even greatly exceed the wavelength of a short-period surface wave. The effect of topography on dispersion data inversion has been studied mainly on the exploration scale (Jin et al., 2022; Koulakov et al., 2016; Li et al., 2019; Nuber et al., 2016). However, these studies all focused on terrestrial areas. Considering the effects of water and topography would be a priority in future research on submarine tomography at shallow depths. Here, we used an approximate method to invert the 1-D regional average S-wave velocity by minimizing the influence of topography. First, we chose stations in a region with no significant difference in elevation. We thus divided the study area into three parts labeled as incoming plate, forearc, and rifting region (Figure 1b). On the other hand, the interstation distance must be greater than two wavelengths and 5 times the maximum elevation difference along the path: $\Delta > 2\lambda = 2ct > 5\Delta_{\text{topo}}$. Periods are limited to meeting the far-field requirement and simultaneously ignoring the topography relief.

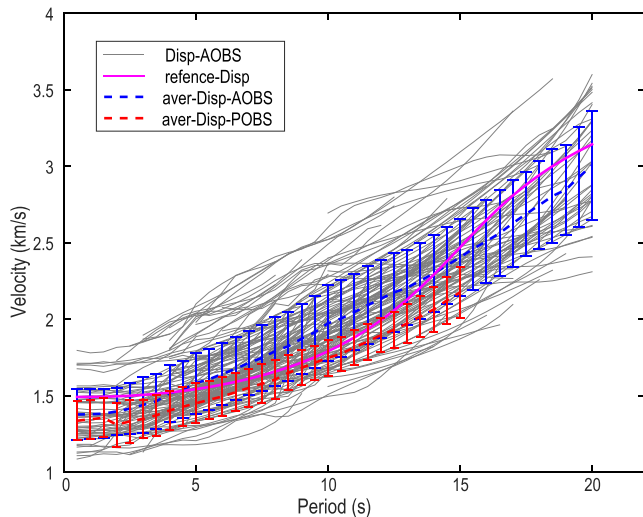


Figure 8. Rayleigh wave phase velocity dispersion curves obtained from the AOBs data (gray lines). The blue dashed line with error bars denotes the average dispersion curve with the standard errors. The red dashed line is the average dispersion data from the POBS data in the study area. The pink curve is the modeled phase velocity dispersion curve based on the average initial model from Zhu et al. (2021), as shown in Figure 9b.

Using the average dispersion data, we selected stations inside the three subregions (Figure 1) to perform regional 1-D inversions. The three subregions have different water depths that are added to the same initial model (Figure 9) obtained from Zhu et al. (2021). The forward modeled dispersion curves of the Rayleigh wave phase velocity from the three initial models show significant differences, especially in our concerned period band of 1–20 s (Figure S2 in Supporting Information S1). Since the data is restricted to a small area, the length of the dispersion curve will be limited synchronously (Figure 9a). Long-period dispersion data can be extracted between different regions with longer paths (Figure 8), which can be used in 3-D velocity structure inversion in future studies to handle the realistic topography and water layer effect. For this study, the Rayleigh wave phase velocity sensitivity kernel mainly focused on the shallow lithosphere (Figure S3 in Supporting Information S1). We generated two hundred models based on the initial model by adding a restricted random value to each layer (Figure S4 in Supporting Information S1). The final inverted model was the average of all convergent inversion results with a depth limit of 30 km, as shown in Figure 9. The convergent inverted results from different initial models reveal similar patterns, especially at the most sensitive depths (Figure S4 in Supporting Information S1). The standard deviation ranges from 0.1 to 0.3 km/s at different depths (Figure S4 in Supporting Information S1). Data in the incoming plate and forearc

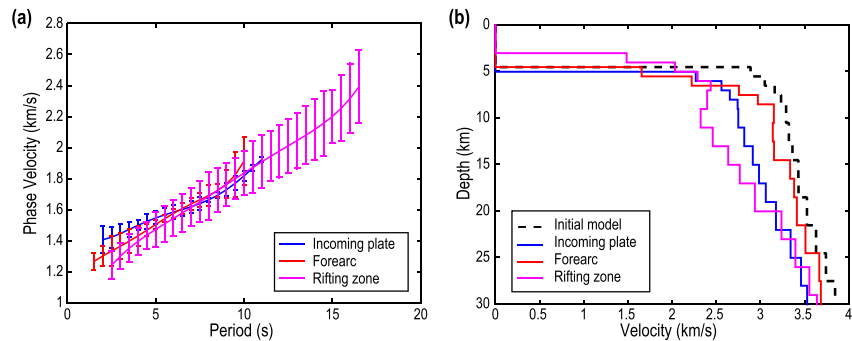


Figure 9. (a) Average Rayleigh wave phase velocity dispersion curves with error bars for different regions denoted by different colors. (b) Initial model (black dashed line) and three inverted models corresponding to the annotation shown in the bottom left. It is worth noting that the water depth in each region's initial model is different.

region lack relatively long period parts. As a result, the inversion of these two regions generally updated shallower depth than the rifting zone.

4. Discussion

4.1. Comparison of the Inverted Models With Previous Studies

The inverted results were compared with previous studies using different data and methods in and around the study area. We first converted the P-wave velocity structure obtained from the active source phases (He et al., 2023; Wan et al., 2019) to S-wave velocity by roughly dividing by 2 due to the possible magmatism and serpentinization (Holbrook et al., 1992). The converted S-wave velocity and results from Zhu et al. (2021) using surface wave tomography of the POBS data were compared with our results. We also included the velocity profile in central Mariana from Cai et al. (2018) in the comparison after adding the same water depths (Figure 10). The comparison was conducted in three different subregions, as marked in Figure 1b, that is, the rifting zone, forearc, and incoming plate, from northwest to southeast of the southernmost Mariana Trench. Considering the different data sets and methods, the S-wave velocity structures above the depth of 25 km are comparable. Due to the data limitations and differences in the study region, only the models from Wan et al. (2019) cover the rifting zone among these previous studies.

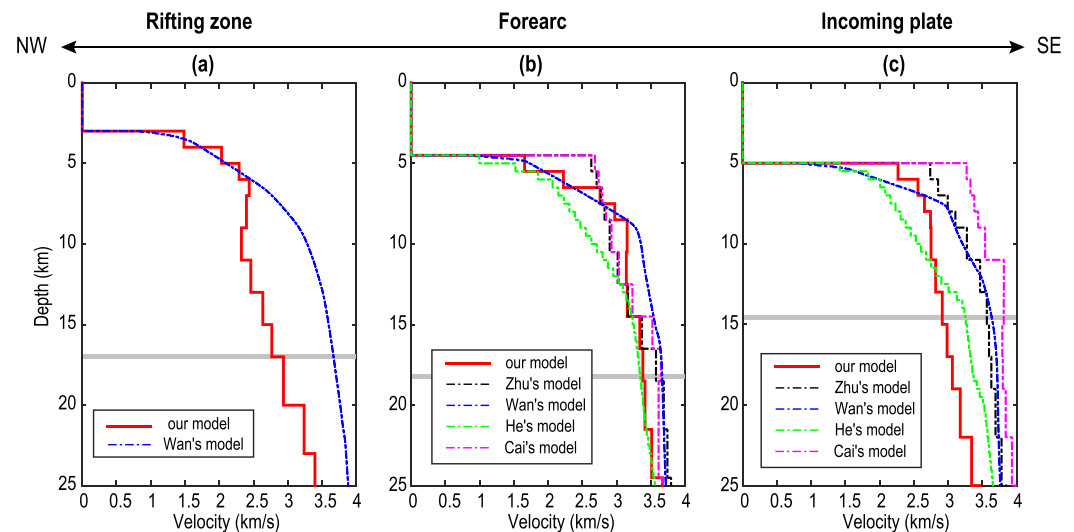


Figure 10. Velocity comparison of three subregions from northwest to southeast of the southernmost Marina Trench as marked in Figure 1b. Different line types denote different models as labeled in each panel. The gray bars represent the Moho depths obtained from Wan et al. (2019).

The shallow parts of the SWMR display a relatively low-velocity anomaly linked to the active rifting here, as evidenced by the morphology and the occurrence of numerous extensional earthquakes (Martinez et al., 2018; Wan et al., 2019). This anomaly is more prominent in our structure and could reach a depth of more than 20 km (Figure 10a). Serpentinization with fluid penetrating from fractures or dehydration from the subducting slab dramatically influences the temperature and velocity. Additionally, the crustal thickness here is greater than that of the forearc region (Wan et al., 2019). Due to the lack of a mature island arc, this rift zone is amagmatic and different from other arc to back-arc basin zones with tectonic spreading (Sleeper et al., 2021). The structure and possible mechanism of the formation of the SWMR still need to be better understood. However, we deduced that the rifting process and likely hydrous minerals might have commonly contributed to this low-velocity anomaly.

The overall increasing trend of the three models appears similar in the forearc region (Figure 10b), which has not undergone extensive extension (Sleeper et al., 2021). This structure has been interpreted by a lower degree of serpentinization compared to the forearc region of the central Mariana Trench, where mud volcanos and serpentine seamounts exist (Cai et al., 2018; Zhu et al., 2021). The apparent difference emerged in the outer-rise region shown in our model, where a low-velocity zone below the seafloor extends into the mantle (Figure 10c). This velocity pattern is stable with different inversion parameters and initial models (Figure S4 in Supporting Information S1). The low-velocity feature also appears at the top of the incoming plate mantle according to the results of Zhu et al. (2021) and Cai et al. (2018). However, our results show much lower velocity compared to other models (Figure 10c), indicating greater hydration than in previous studies (Wan et al., 2019; Zhu et al., 2021). A low-velocity layer beneath the crust, thus interpreted by serpentinization, has also been identified using P-wave velocity tomography in this region (He et al., 2023). Before subduction, the low-velocity zone within the slab should be related to dense and brittle bending-related normal faults that cut through the Moho and allow fluid transport and partial serpentinization at shallow depths (Emry & Wiens, 2015; Emry et al., 2014).

4.2. Water Input Estimation

We roughly estimated the content of water input within the subducted slab based on the velocity model. Apart from the hydration, the influence of water-filled porosity cannot be neglected when studying the velocity reduction of shallow parts of the slab before subduction. The porosity decreases along depth due to increased pressure. In central Mariana, the velocity reduction due to pore water in cracks is ~ 0.3 km/s by comparing the shallow and deep parts of the subducting slab (Cai et al., 2018), which was also used in our estimation. At shallow depths, we chose the experimental relationship between the S-wave velocity and low-temperature serpentine form (lizardite and chrysotile):

$$V_s = 4.51 - 2.19 \times \Phi \quad (3)$$

where Φ is the serpentine volume fraction (Ji et al., 2013). Previous studies show that the crustal thickness of the incoming plate is ~ 7 – 8 km (Wan et al., 2019; Zhu et al., 2021). The low velocities of ~ 2.9 – 3.6 km/s in the uppermost mantle indicate serpentinization of ~ 28 – 60 vol% (i.e., ~ 3.0 – 6.9 wt%) after removal of the influence of pore water, which significantly exceeds the estimation ~ 19 – 41 vol% from Zhu et al. (2021). At the same depth as the incoming plate of the central Mariana Trench, the low velocity anomaly is ~ 3.8 km/s (Figure 10), indicating ~ 19 vol% serpentinization (Cai et al., 2018). Several geodynamic modeling studies at the Mariana Trench indicate that the water content of the subducting slab in the southern part should be greater than that of the northern and central Mariana Trench (Zhang et al., 2021; Zhou & Lin, 2018; Zhou et al., 2015). The difference might reach about twice as much water being carried into the mantle per unit of trench length (Zhou & Lin, 2018), corresponding to our estimation. It should be noted that, the uncertainty of the inverted structure would influence the estimation to a certain degree ($\sim \pm 10$ vol%), which does not conflict with the implication of more water input.

The hydrated layer's thickness influenced by the depth extent of faults is still controversial in Mariana, which determines the water content directly. The tomographic results in the central and southernmost Mariana reveal similar ~ 25 -km-thick slab-mantle layers, determined by the velocity contour of 4.1 km/s bounding the serpentinization depth (Cai et al., 2018; Zhu et al., 2021). However, the depths of normal fault penetration from numerical modeling and earthquake relocation differ from northern to southern Mariana (Chen et al., 2022; Eimer et al., 2020; Emry et al., 2014; Zhou & Lin, 2018). These faults extend to ~ 20 km in the north and central part but penetrate deeper than 30 km in the south based on geodynamic modeling (Zhou & Lin, 2018). Furthermore, an outer-rise event cluster identified via machine learning using OBS data revealed an outer-rise fault penetrating to

a depth of 50 km in the southern part (Chen et al., 2022). These studies all support a deeper penetration depth in the south Mariana Trench. Although our result cannot tell the whole thickness of the serpentinized layer as it has not reached the bound of 4.1 km/s in the sensitive depth range (Figure 9), the seismic data indicate that the hydrate layer should be thicker than 25 km and contain more water deduced from reasonable speculation.

4.3. Method Assessment

The combination of short-segment cross-correlation and the selected tf-PWS can significantly improve the quality of NCFs using the AOBS data. The extracted dispersion curves can then be used to invert S-wave velocity structures of shallow depths due to the small aperture of AOBS, which would greatly complement marine tectonic studies. After combining the inverted P-wave velocity structures using the active phase, the velocity ratio of P and S waves could be obtained, which is critical for investigating subseafloor tectonic processes. However, direct division is not recommended because different data sets and methodologies may generate systematic differences, resulting in unreasonable values. Moreover, our approach can also be practical for long inter-station distances of the AOBS data, which shield valid NCFs over 400 km apart using the recorded ambient noise (Figure 6d). Thus, the extracted dispersion data could also be used to invert deep structures.

It is worth noting that the effective period range of the seismic instruments should comprise the period band that can be used in ambient noise tomography, as many short-period instruments employed in active source experiments may not be suitable for this method. The time length of the AOBS data is another factor that may affect the quality of the results. As shown in Figure 3a, the SNR does not change much after about 1 week's stacking. Data with a record of only a few days can also be used, although the parameters used for correlation and stacking should be tested.

We included a few off-profile stations in this processing to increase the dispersion data and expand the data coverage. Due to the sharp fluctuation of the seafloor topography of the study region, the along-profile stations inside each subregion are rare and too close, resulting in few dispersion data obtained for subsequent inversion, especially for long periods. Therefore, the utilization of off-profile stations is only a supplement to the final velocity inversion of this work. This method can be universal for AOBS data within a relatively flat area or after incorporating the realistic effects of the water layer and topographic relief through a new inversion strategy.

For the POBS data, adopting our method can generate high-quality Green's functions (Figure 6c, Figures S1a and S1b in Supporting Information S1), which can be used for more precise structural inversion. The correlated waveform can be the objective function as the source at one station and receive waveform at the other. Other methods, such as the spectral element method (Jin et al., 2022), can be used to obtain a more accurate model concerning the various topographies and water layers.

5. Conclusions

We developed a workflow for processing the AOBS data using ambient noise interferometry by combining methods of short-segment cross-correlation and selected tf-PWS to generate high-quality NCFs. The stacked result can be used to invert the S-wave velocity structure when the data comprise the objective period band. This method could reutilize the existing AOBS data and detect more information about subseafloor structures, which could be essential supplements to previous studies. We applied the new approach to the AOBS data set acquired in the southernmost Mariana Trench and inverted 1-D S-wave velocity structures for regions without considerable topographic relief. The inverted structures have been compared with other research conducted in the study area and provide new perspectives on the tectonics of the shallow part of the southern Mariana subduction zone, especially the newly detected low-velocity zone in the outer rise region, indicating more hydration than previously estimated. When applied to POBS data, the cleaned and high-quality NCFs can also be used as the objective functions of waveform modeling concerning the actual water depth and topographic variations. Following this way, more concise 3-D subseafloor structures and widely used methods can be achieved in the near future.

Data Availability Statement

The waveform data can be found in Wan et al. (2019) and Zhu et al. (2021). The calculated ambient noise cross-correlation data and velocity models generated from this study are available at (Zhang, 2023). All figures and analyses were performed using GMT (<https://www.generic-mapping-tools.org>) and MATLAB (<https://www.mathworks.com/products/matlab.html>).

Acknowledgments

The authors appreciate the editor Michael Bostock, the associate editor and two anonymous reviewers for their assistance in promoting this study. We also thank the captain, crew, and scientific party of the R/V *Shiyun 3* Mariana Trench Cruise for their tremendous efforts during the OBS experiments. We are grateful to Gaohua Zhu and Chen Cai for sharing their published models. This research was supported by the National Natural Science Foundation of China (91858207, 41890813, 42304068, and 42104104), Hainan Provincial Joint Project of Sanya Yazhou Bay Science and Technology City (120LH014), Guangdong Basic and Applied Basic Research Foundation (2021B1515020023, 2022A1515110933), Chinese Academy of Sciences (Y4SL021001, QYZDY-SSW-DQC005, and 133244KYSB20180029), and Shenzhen Science and Technology Innovation Commission (JCYJ20220818100417038 and KCXFZ20211020174803005). H. Yang was sponsored by Hong Kong Research Grant Council Grants (14304820) and the National Natural Science Foundation of China (92158205). Y. Zhang and C. Yu were also supported by the Guangzhou Basic and Applied Basic Research Foundation (2023A04J0190, 202201010637).

References

Abbas, A., Zhu, G., Zi, J., Chen, H., & Yang, H. (2022). Evaluating and correcting short-term clock drift in data from temporary seismic deployments. *Earthquake Research Advances*, 3(2), 100199. <https://doi.org/10.1016/j.eqrea.2022.100199>

Afonin, N., Kozlovskaya, E., Nevalainen, J., & Narkilahti, J. (2019). Improving the quality of empirical Green's functions, obtained by cross-correlation of high-frequency ambient seismic noise. *Solid Earth*, 10(5), 1621–1634. <https://doi.org/10.5194/se-10-1621-2019>

Ardhuin, F., Gualtieri, L., & Stutzmann, E. (2015). How ocean waves rock the Earth: Two mechanisms explain microseisms with periods 3 to 300 s. *Geophysical Research Letters*, 42, 765–772. <https://doi.org/10.1002/2014GL062782>

Bensen, G. D., Ritzwoller, M. H., Barmin, M. P., Levshin, A. L., Lin, F., Moschetti, M. P., et al. (2007). Processing seismic ambient noise data to obtain reliable broad-band surface wave dispersion measurements. *Geophysical Journal International*, 169(3), 1239–1260. <https://doi.org/10.1111/j.1365-246X.2007.03374.x>

Cai, C., Wiens, D. A., Shen, W., & Eimer, M. (2018). Water input into the Mariana subduction zone estimated from ocean-bottom seismic data. *Nature*, 563(7731), 389–392. <https://doi.org/10.1038/s41586-018-0655-4>

Chen, H., Yang, H., Zhu, G., Xu, M., Lin, J., & You, Q. (2022). Deep outer-rise faults in the Southern Mariana Subduction Zone indicated by a machine-learning-based high-resolution earthquake catalog. *Geophysical Research Letters*, 49(12), e2022GL097779. <https://doi.org/10.1029/2022GL097779>

Cheng, F., Xia, J., Ajo-Franklin, J. B., Behm, M., Zhou, C., Dai, T., et al. (2021). High-resolution ambient noise imaging of geothermal reservoir using 3C dense seismic nodal array and ultra-short observation. *Journal of Geophysical Research: Solid Earth*, 126(8), e2021JB021827. <https://doi.org/10.1029/2021JB021827>

Cheng, F., Xia, J., Xu, Y., Xu, Z., & Pan, Y. (2015). A new passive seismic method based on seismic interferometry and multichannel analysis of surface waves. *Journal of Applied Geophysics*, 117, 126–135. <https://doi.org/10.1016/j.jappgeo.2015.04.005>

Eimer, M., Wiens, D. A., Cai, C., Lizarralde, D., & Jaspersen, H. (2020). Seismicity of the incoming plate and forearc near the Mariana Trench recorded by ocean bottom seismographs. *Geochemistry, Geophysics, Geosystems*, 21(4), e2020GC008953. <https://doi.org/10.1029/2020gc008953>

Emry, E. L., & Wiens, D. A. (2015). Incoming plate faulting in the Northern and Western Pacific and implications for subduction zone water budgets. *Earth and Planetary Science Letters*, 414, 176–186. <https://doi.org/10.1016/j.epsl.2014.12.042>

Emry, E. L., Wiens, D. A., & Garcia-Castellanos, D. (2014). Faulting within the Pacific plate at the Mariana Trench: Implications for plate interface coupling and subduction of hydrous minerals. *Journal of Geophysical Research: Solid Earth*, 119(4), 3076–3095. <https://doi.org/10.1002/2013JB010718>

He, E., Qiu, X., Chen, C., Wang, Y., Xu, M., Zhao, M., & You, Q. (2023). Deep crustal structure across the Challenger Deep: Tectonic deformation and strongly serpentinized layer. *Gondwana Research*, 118, 135–152. <https://doi.org/10.1016/j.gr.2023.02.020>

Herrmann, R. B. (2013). Computer programs in seismology: An evolving tool for instruction and research. *Seismological Research Letters*, 84(6), 1081–1088. <https://doi.org/10.1785/0220110096>

Holbrook, W. S., Mooney, W. D., & Christensen, N. I. (1992). The seismic velocity structure of the deep continental crust. *Continental Lower Crust*, 23, 1–43.

Huang, H., Qiu, X., Zhang, J., & Hao, T. (2019). Low-velocity layers in the northwestern margin of the South China Sea: Evidence from receiver functions of ocean-bottom seismometer data. *Journal of Asian Earth Sciences*, 186, 104090. <https://doi.org/10.1016/j.jseas.2019.104090>

Ji, S., Li, A., Wang, Q., Long, C., Wang, H., Marcotte, D., & Salisbury, M. (2013). Seismic velocities, anisotropy, and shear-wave splitting of antigorite serpentinites and tectonic implications for subduction zones. *Journal of Geophysical Research: Solid Earth*, 118(3), 1015–1037. <https://doi.org/10.1002/jgrb.50110>

Jin, R., He, X., Fang, H., Xie, J., Liu, Y., & Zhang, P. (2022). Topography effect on ambient noise tomography: A case study for the Longmen Shan area, eastern Tibetan Plateau. *Geophysical Journal International*, 233(1), 1–12. <https://doi.org/10.1093/gji/ggac435>

Koulakov, I., Maksotova, G., Jaxybulatov, K., Kasatkina, E., Shapiro, N. M., Luehr, B.-G., et al. (2016). Structure of magma reservoirs beneath Merapi and surrounding volcanic centers of Central Java modeled from ambient noise tomography. *Geochemistry, Geophysics, Geosystems*, 17(10), 4195–4211. <https://doi.org/10.1002/2016GC006442>

Le, B. M., Yang, T., & Morgan, J. P. (2022). Seismic constraints on crustal and uppermost mantle structure beneath the Hawaiian Swell: Implications for plume-lithosphere interactions. *Journal of Geophysical Research: Solid Earth*, 127(11), e2021JB023822. <https://doi.org/10.1029/2021JB023822>

Li, J., Lin, F.-C., Allam, A., Ben-Zion, Y., Liu, Z. L., & Schuster, G. (2019). Wave equation dispersion inversion of surface waves recorded on irregular topography. *Geophysical Journal International*, 217(1), 346–360. <https://doi.org/10.1093/gji/ggz005>

Liu, D., Yang, T., Le, B., Wu, Y., Wang, Y., Huang, X., et al. (2022). Seismometer-detached broadband ocean bottom seismograph (OBS): Development, test, and data quality analysis (in Chinese with English abstract). *Chinese Journal of Geophysics*, 65(7), 2560–2572. <https://doi.org/10.6036/cjg2022P0441>

Liu, Y., Xia, J., Xi, C., Dai, T., & Ning, L. (2021). Improving the retrieval of high-frequency surface waves from ambient noise through multichannel-coherency-weighted stack. *Geophysical Journal International*, 227(2), 776–785. <https://doi.org/10.1093/gji/ggab253>

Martinez, F., Stern, R. J., Kelley, K. A., Ohara, Y., Sleeper, J. D., Ribeiro, J. M., & Brounce, M. (2018). Diffuse extension of the southern Mariana margin. *Journal of Geophysical Research: Solid Earth*, 123(1), 892–916. <https://doi.org/10.1002/2017JB014684>

Mjelde, R., Raum, T., Digranes, P., Shimamura, H., Shiobara, H., & Kodaira, S. (2003). Vp/Vs ratio along the Vøring margin, NE Atlantic, derived from OBS data: Implications on lithology and stress field. *Tectonophysics*, 369(3–4), 175–197. [https://doi.org/10.1016/S0040-1951\(03\)00198-7](https://doi.org/10.1016/S0040-1951(03)00198-7)

Mordret, A., Landès, M., Shapiro, N. M., Singh, S. C., & Roux, P. (2014). Ambient noise surface wave tomography to determine the shallow shear velocity structure at Valhall: Depth inversion with a Neighbourhood Algorithm. *Geophysical Journal International*, 198(3), 1514–1525. <https://doi.org/10.1093/gji/ggu217>

Moreau, L., Stehly, L., Boue, P., Lu, Y., Larose, E., & Campillo, M. (2017). Improving ambient noise correlation functions with an SVD-based Wiener filter. *Geophysical Journal International*, 211(1), 418–426. <https://doi.org/10.1093/gji/ggx306>

Nuber, A., Manukyan, E., & Maurer, H. (2016). Ground topography effects on near-surface elastic full waveform inversion. *Geophysical Journal International*, 207(1), 67–71. <https://doi.org/10.1093/gji/ggw267>

Prieto, G. A., Lawrence, J. F., & Beroza, G. C. (2009). Anelastic earth structure from the coherency of the ambient seismic field. *Journal of Geophysical Research*, 114(B7), B07303. <https://doi.org/10.1029/2008JB006067>

Qiao, Q., Liu, X., Zhao, D., Li, S., Zhao, S., Zhao, L., & Wang, X. (2021). Upper mantle structure beneath Mariana: Insights from Rayleigh-wave anisotropic tomography. *Geochemistry, Geophysics, Geosystems*, 22(11), e2021GC009902. <https://doi.org/10.1029/2021GC009902>

- Schimmel, M., Stutzmann, E., & Gallart, J. (2011). Using instantaneous phase coherence for signal extraction from ambient noise data at a local to a global scale. *Geophysical Journal International*, *184*(1), 494–506. <https://doi.org/10.1111/j.1365-246X.2010.04861.x>
- Seats, K. J., Lawrence, J. F., & Prieto, G. A. (2012). Improved ambient noise correlation functions using Welch's method. *Geophysical Journal International*, *188*(2), 513–523. <https://doi.org/10.1111/j.1365-246X.2011.05263.x>
- Shapiro, N. M., & Campillo, M. (2004). Emergence of broadband Rayleigh waves from correlations of the ambient seismic noise. *Geophysical Research Letters*, *31*(7), L07614. <https://doi.org/10.1029/2004GL019491>
- Sleeper, J. D., Martinez, F., Fryer, P., Stern, R. J., Kelley, K. A., & Ohara, Y. (2021). Diffuse spreading, a newly recognized mode of crustal accretion in the southern Mariana Trough backarc basin. *Geosphere*, *17*(5), 1382–1404. <https://doi.org/10.1130/GES02360.1>
- Stockwell, R. G., Mansinha, L., & Lowe, R. P. (1996). Localization of the complex spectrum: The S transform. *IEEE Transactions on Signal Processing*, *44*(4), 998–1001. <https://doi.org/10.1109/78.492555>
- Takahashi, N., Kodaira, S., Tatsumi, Y., Kaneda, Y., & Suyehiro, K. (2008). Structure and growth of the Izu-Bonin-Mariana arc crust: 1. Seismic constraint on crust and mantle structure of the Mariana arc-back-arc system. *Journal of Geophysical Research*, *113*(1), 1–18. <https://doi.org/10.1029/2007JB005120>
- Tian, J., Lin, J., Zhang, F., Xu, M., Zhang, Y., Guo, L., & Zeng, X. (2021). Time correction of ocean-bottom seismometers using improved ambient noise cross correlation of multicomponents and dual-frequency bands. *Seismological Research Letters*, *92*(3), 2004–2014. <https://doi.org/10.1785/0220200358>
- Wan, K., Lin, J., Xia, S., Sun, J., Xu, M., Yang, H., et al. (2019). Deep seismic structure across the southernmost Mariana Trench: Implications for arc rifting and plate hydration. *Journal of Geophysical Research: Solid Earth*, *124*(5), 4710–4727. <https://doi.org/10.1029/2018JB017080>
- Weeraratne, D. S., Forsyth, D. W., Yang, Y., & Webb, S. C. (2007). Rayleigh wave tomography beneath intraplate volcanic ridges in the South Pacific. *Journal of Geophysical Research*, *112*(B6), B06303. <https://doi.org/10.1029/2006JB004403>
- Welch, P. D. (1967). The use of fast Fourier transform for the estimation of power spectra: A method based on time-averaging over short, modified periodograms. *IEEE Transactions on Audio and Electroacoustics*, *15*(2), 70–73. <https://doi.org/10.1109/tau.1967.1161901>
- Wolfe, C. J., Solomon, S. C., Laske, G., Collins, J. A., Detrick, R. S., Orcutt, J. A., et al. (2009). Mantle shear-wave velocity structure beneath the Hawaiian hot spot. *Science*, *326*(5958), 1388–1390. <https://doi.org/10.1126/science.1180165>
- Xie, J., Yang, Y., & Luo, Y. (2020). Improving cross-correlations of ambient noise using an rms-ratio selection stacking method. *Geophysical Journal International*, *222*(2), 989–1002. <https://doi.org/10.1093/gji/ggaa232>
- Yao, H., Gouedard, P., Collins, J. A., McGuire, J. J., & van der Hilst, R. D. (2011). Structure of young East Pacific Rise lithosphere from ambient noise correlation analysis of fundamental-and higher-mode Scholte-Rayleigh waves. *Comptes Rendus Geoscience*, *343*(8), 571–583. <https://doi.org/10.1016/j.crte.2011.04.004>
- Yao, H., van Der Hilst, R. D., & De Hoop, M. V. (2006). Surface-wave array tomography in SE Tibet from ambient seismic noise and two-station analysis-I. Phase velocity maps. *Geophysical Journal International*, *166*(2), 732–744. <https://doi.org/10.1111/j.1365-246X.2006.03028.x>
- Zhang, J., Zhang, F., Lin, J., & Yang, H. (2021). Yield failure of the subducting plate at the Mariana Trench. *Tectonophysics*, *814*, 228944. <https://doi.org/10.1016/j.tecto.2021.228944>
- Zhang, Y. (2023). NCFs from AOBs and POBS data in the southernmost Mariana Trench [Dataset]. *Zenodo*. <https://doi.org/10.5281/zenodo.7614813>
- Zhang, Y., Yao, H., Xu, M., & Liu, B. (2022). Radial anisotropy in the crust beneath Fujian and the Taiwan strait from direct surface-wave tomography. *Tectonophysics*, *827*, 229270. <https://doi.org/10.1016/j.tecto.2022.229270>
- Zhang, Y., Yao, H., Yang, H.-Y., Cai, H.-T., Fang, H., Xu, J., et al. (2018). 3-D crustal shear-wave velocity structure of the Taiwan Strait and Fujian, SE China, revealed by ambient noise tomography. *Journal of Geophysical Research: Solid Earth*, *123*(9), 8016–8031. <https://doi.org/10.1029/2018jb015938>
- Zhou, Z., & Lin, J. (2018). Elasto-plastic deformation and plate weakening due to normal faulting in the subducting plate along the Mariana Trench. *Tectonophysics*, *734–735*, 59–68. <https://doi.org/10.1016/j.tecto.2018.04.008>
- Zhou, Z., Lin, J., Behn, M. D., & Olive, J.-A. (2015). Mechanism for normal faulting in the subducting plate at the Mariana Trench. *Geophysical Research Letters*, *42*(11), 4309–4317. <https://doi.org/10.1002/2015gl063917>
- Zhu, G., Wiens, D. A., Yang, H., Lin, J., Xu, M., & You, Q. (2021). Upper mantle hydration indicated by decreased shear velocity near the southern Mariana Trench from Rayleigh wave tomography. *Geophysical Research Letters*, *48*(15), e2021GL093309. <https://doi.org/10.1029/2021GL093309>
- Zhu, G., Yang, H., Lin, J., Zhou, Z., Xu, M., Sun, J., & Wan, K. (2019). Along-strike variation in slab geometry at the southern Mariana subduction zone revealed by seismicity through ocean bottom seismic experiments. *Geophysical Journal International*, *218*(3), 2122–2135. <https://doi.org/10.1093/gji/ggz272>